Wind and Structures, Vol. 4, No. 5 (2001) 413-440
DOI: http://dx.doi.org/10.12989/was.2001.4.5.413

Unsteady wind loading on a wall

C. J. Baker†

School of Civil Engineering, The University of Birmingham, Edgbaston, Birmingham B15 2TT, U.K.

Abstract. This paper presents an extensive analysis of unsteady wind loading data on a 18 m long and 2 m high wall in a rural environment, with the wind at a range of angles to the wall normal. The data is firstly analyzed using standard statistical techniques (moments of probability distributions, auto- and cross-correlations, auto- and cross-spectra etc.). The analysis is taken further using a variety of less conventional methods - conditional sampling, proper orthogonal decomposition and wavelet analysis. It is shown that, even though the geometry is simple, the nature of the unsteady flow is surprisingly complex. The fluctuating pressures on the front face of the wall are to a great extent caused by the turbulent fluctuations in the upstream flow, and reflect the oncoming flow structures. The results further suggest that there are distinct structures in the oncoming flow with a variety of scales, and that the second order quasi-steady approach can predict the pressure fluctuations quite well. The fluctuating pressures on the rear face are also influenced by the fluctuations in the oncoming turbulence, but also by unsteady fluctuations due to wake unsteadiness. These fluctuations have a greater temporal and spatial coherence than on the front face and the quasi-steady method over-predicts the extent of these fluctuations. Finally the results are used to check some assumptions made in the current UK wind loading code of practice.

Key words: unsteady loading; correlations; proper orthogonal decomposition; wavelet analysis; conditional sampling; wall.

1. Introduction

One of the simplest of bluff body shapes is a two dimensional wall mounted onto a surface, and such a configuration has often been investigated by experimenters in the past using wind tunnel models (e.g., Letchford and Holmes 1994). However such investigations are of somewhat limited value in terms of wind engineering because the small scale of the experiments introduces Reynolds number effects, and the simulated wind tunnel boundary layer cannot be fully representative of atmospheric boundary layer conditions very close to the ground. To obtain data that were not compromised by such modelling effects, Silsoe Research Institute have carried out wind loading experiments on a full scale experimental wall of variable geometry. These experiments are reported in Robertson *et al.* (1996a,b, 1997). They were primarily carried out to enable time mean loading data to be obtained for different wall geometries, for inclusion in design codes of practice, and to a large extent the analysis that has been carried out to date has been to meet these requirements. Robertson *et al.* (1997) extended this somewhat to investigate the relationship between unsteady pressures and unsteady overall forces. In this paper the unsteady wind loading characteristics on this structure will be considered, firstly using standard statistical methods of analysis (moments of

† Professor

probability distributions, auto- and cross-correlations, power spectra etc) and secondly using less standard techniques (POD, conditional sampling and wavelet analysis). It will be seen that despite the relatively simple geometry of the situation the unsteady flow field is very complex indeed. This paper will attempt to unravel some of these complexities. The data that will be presented will also form a useful dataset for the validation of unsteady CFD codes using, for example, the LES technique. If such methods are to be useful within the field of wind engineering, then there is a need for them to be able to predict unsteady wind characteristics and loading parameters, and the results presented here, for the simple geometric case of a two dimensional wall, should be useful in this respect.

The experimental details are set out in section 2. Section 3 then sets out the results of an analysis carried out using conventional methods (moments of probability distributions, auto-correlations and cross-correlations and power spectra). Sections 4, 5 and 6 then present less conventional types of analysis of the data - conditional sampling, POD (Proper Orthogonal Decomposition) and wavelet analysis respectively. Section 7 then attempts to synthesise the results, and to arrive at a coherent description of the unsteady flow field around the wall. Finally some concluding remarks are set out in section 8.

2. The experiments

The experimental wall was constructed out of 2 m square panels, with pressure tappings at the centre of the front and the back of the panel. These could be positioned end to end to form walls of variable lengths. Return corners could also be added. Full details are given in Robertson *et al*. (1996a,b, 1997). The wall was positioned at the well documented Silsoe experimental site, where the boundary layer and turbulence characteristics have been measured over a number of years. Details of the nature of the wind structure at that site are given in Hoxey and Richards (1992). It is essentially a rural site with a surface roughness length of 0.01 m and a power law exponent of 0.15. Further details of the spectral characteristics of the flow are given in Richards *et al*. (1997). The experimental data that will be considered in this paper was obtained for one specific wall geometry with 9 panels and no return corners, i.e., an 18 m $\times$ 2 m wall. Three specific datasets will be used, with different wind directions relative to the wall. The experimental conditions for these datasets are summarised in Table 1. The first two of the datasets listed in Table 1 are sixty minutes in length (i.e., 18000 data points for each velocity component and pressure tapping), whilst the third is 30 minutes in length. These were measured with a reference sonic anemometer mounted at wall height,

Table 1 Experimental conditions

Direction	-1.2^o	17.1^o	38.1^o
U m/s	9.68	10.11	8.62
σ_u/U	0.283	0.237	0.254
σ_v/U	0.218	0.188	0.223
σ_w/U	0.092	0.085	0.089
u_τ/U	0.088	0.083	0.077
s_u	0.424	0.336	0.599
s_v	0.129	0.056	0.195
s_w	0.059	0.140	0.206
s_q	1.183	1.003	1.319
U_e/U	2.02	1.85	2.04

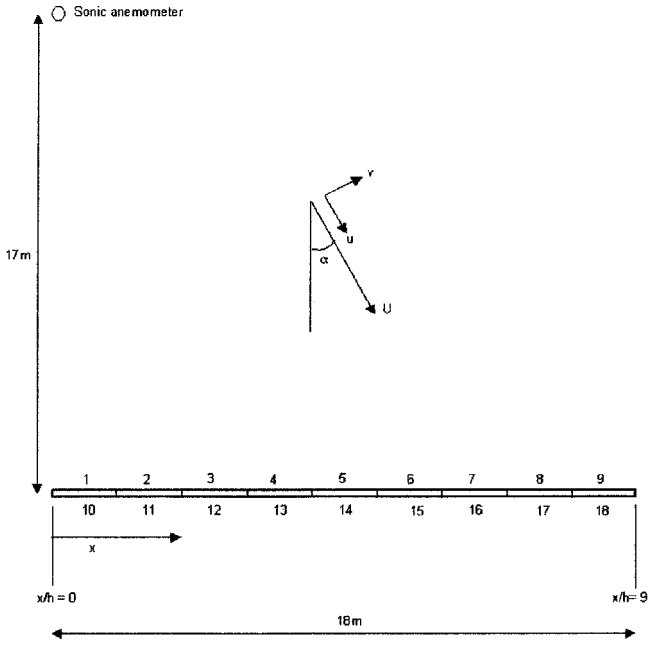

Fig. 1 Schematic plan view of the experimental wall (numbers represent pressure tappings)

17 m upwind of one end of the wall, with a sampling rate of 5 Hz (Fig. 1). The table gives the mean wind speed U, the three turbulence intensities σ_u, σ_v and σ_w, the dimensionless friction velocity u_τ/U, the skewnesses of the three velocity component distributions s_u, s_v, and s_w, the skewness of the dynamic pressure s_q, and the ratio of the extreme wind speed to the mean wind speed U_e/U. This extreme wind speed is the 99.95th percentile for the first two datasets, and the 99.9th percentile for the third, which all correspond to the maximum 1.8s of the dataset. Wind direction (α) is specified with respect to the wall normal i.e., 0° wind direction is normal to the wall, and 90° is parallel to the wall. The u component is parallel to the mean flow direction, the v component is horizontal and perpendicular to the mean flow direction, and the w component is in the vertical direction. In what follows the results will be presented for 18 pressure tappings. Tappings 1 to 9 are on the windward face of the wall, with tapping 1 at the "leading edge" for non-normal wind directions. If h is the wall height, and x is the distance from the end of the wall, these tappings are thus at a height of $h/2$, and at dimensionless distances $x/h = 0.5, 1.5, 2.5 \ldots 8.5$ from the end of the wall. Tappings 10 to 18 are on the leeward face of the wall, with tapping 10 being behind tapping 1 etc. (Fig. 1). The pressures were sampled at 5 Hz, with the static reference measured at the anemometer position. The division of the datasets into 10 minute intervals and the calculation of the mean and standard deviation for each interval, revealed no discernible drift in the data during the course of the collection period.

From Table 1 it can be seen that for the three runs being considered, the first has a mean wind direction (α) close to the wall normal (-1.2°), and the other two are at significant angles to the normal (17.1° and 38.1°). The mean velocity in all three cases is around 10 m/s, and the three turbulence intensities in the longitudinal, lateral and vertical directions and the Reynolds stress are also similar in each case. These values are consistent with the values that would be expected over rural terrain (ESDU 1985). The ratio of the extreme value to the mean value is around 2.0 in each case.

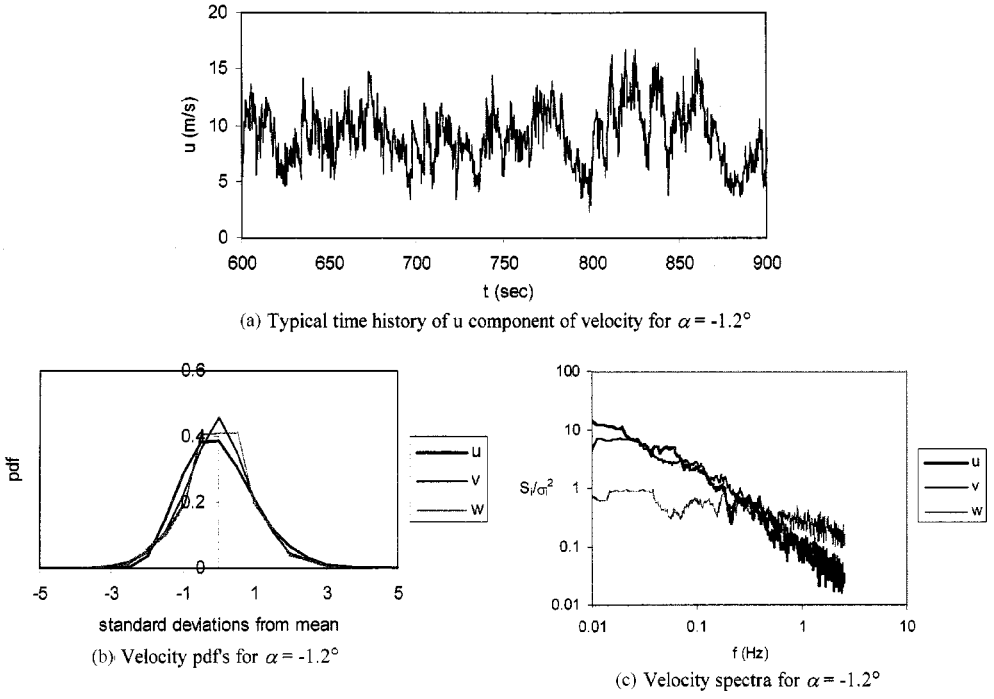

(a) Typical time history of u component of velocity for $\alpha = -1.2°$

(b) Velocity pdf's for $\alpha = -1.2°$

(c) Velocity spectra for $\alpha = -1.2°$

Fig. 2 Characteristics of upstream wind conditions

A typical *u* velocity time series is shown in Fig. 2a. Perhaps the most notable features are the discrete short duration "spikes" in the time series associated with extreme events. This results in non-zero skewness for this velocity component (0.3 to 0.6). The skewness is however rather smaller for the other velocity components. This skewness is also apparent in the probability distribution functions for the wind velocity components shown in Fig. 2b, where a long positive tail to the longitudinal velocity component can be discerned.

Fig. 2c shows the power spectra for the wind velocity components for the -1.2° case (although the results for the other cases are very similar). The spectral density for each component (S_u , S_v, S_w) divided by its variance (σ_u^2 , σ_v^2, σ_w^2) is plotted against frequency *f*. The inertial subrange is very clearly seen at the higher frequencies for the *u* and *v* spectra. The slope of the curves at high frequencies (above about 0.5 Hz) are close to the expected (-5/3) value. This is consistent with the results of Richards *et al.* (1997) for data from the same site, who identified a "power law" region between frequencies of 0.01 to 0.5 Hz that was effectively a transition between a low frequency region of constant spectral density and the high frequency inertial sub range. The *w* spectrum shows a significant amount of energy at the higher frequencies.

3. Analysis of results by conventional methods

The mean pressure coefficient distributions are shown in Fig. 3. These are defined by the equation

$$C_p = \frac{p - p_r}{0.5\rho U^2} \tag{1}$$

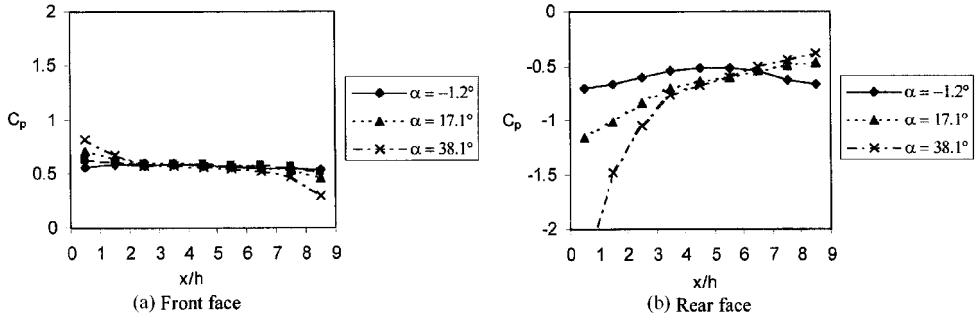

Fig. 3 Mean pressure coefficients

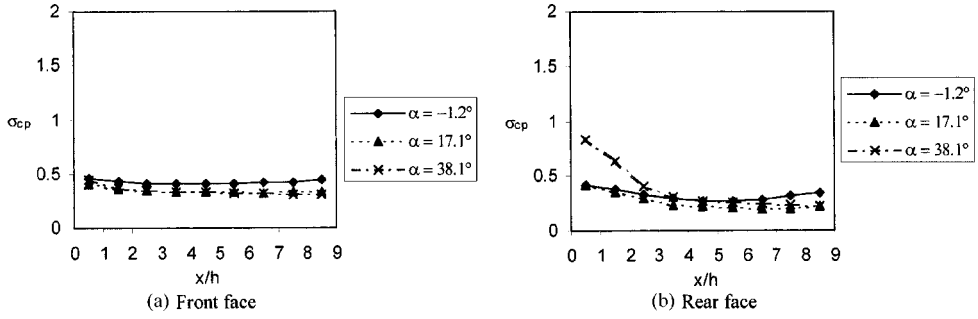

Fig. 4 Standard deviations of pressure coefficients

where p is the mean surface pressure, p_r is the reference pressure and ρ is the density of air. The coefficients can be seen to be uniform for wind normal to the wall, but large spanwise pressure gradients develop for non-normal wind directions, particularly on the rear face. The mean coefficient at the rear of the leading edge of the wall for the highest flow incidence is less than -2, and probably results from a vigorous separated flow in that region. The pressure coefficient standard deviations (σ_{cp}) in Fig. 4 broadly reflect the mean pressure distributions, with the highest values in the lee of the wall at the highest angle of incidence. The skewnesses of Fig. 5 (s_{cp}) depart significantly from zero with magnitudes of around 1 to 1.5. An examination of the individual time series of pressure coefficients show that the largest coefficients are associated with relatively short duration peaks of an intermittent nature and it is these peaks that lead to the high skewnesses (Fig. 6a). These peaks are similar to some degree to peaks in the upstream velocity time histories and the values of the pressure coefficient skewnesses, at least on the windward wall, are close to the value of the skewness of the dynamic pressure in Table 1. This is further illustrated in the pdf's of pressure coefficient in Figs. 6b and 6c. Only values at the centre of the wall ($x / h = 4.5$) on the front and the rear are shown, but the plots for other points are very similar. It can be seen that there is a long positive tail for the front face pressure coefficients, and a long negative tail for the rear face pressure coefficients.

Fig. 7 shows the distributions of the extreme values of pressure coefficient (C_{pe}). This is the 99.95th percentile for $\alpha = -1.2^o$ and 17.1^o, and the 99.9th percentile for $\alpha = 38.1^o$, all of which correspond to the maximum 1.8s of the data. Again these are uniform for near normal wind directions, but become very asymmetric for non-normal directions. Very high suction values in the lee of the leading edge can be observed at the highest angle of incidence. These extreme values

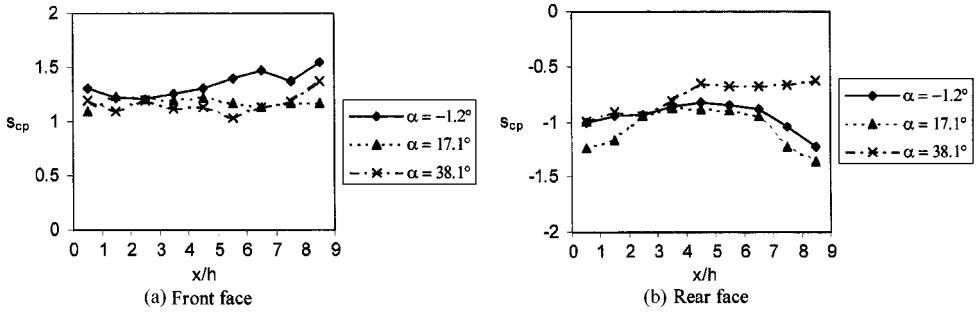

Fig. 5 Pressure coefficient skewness

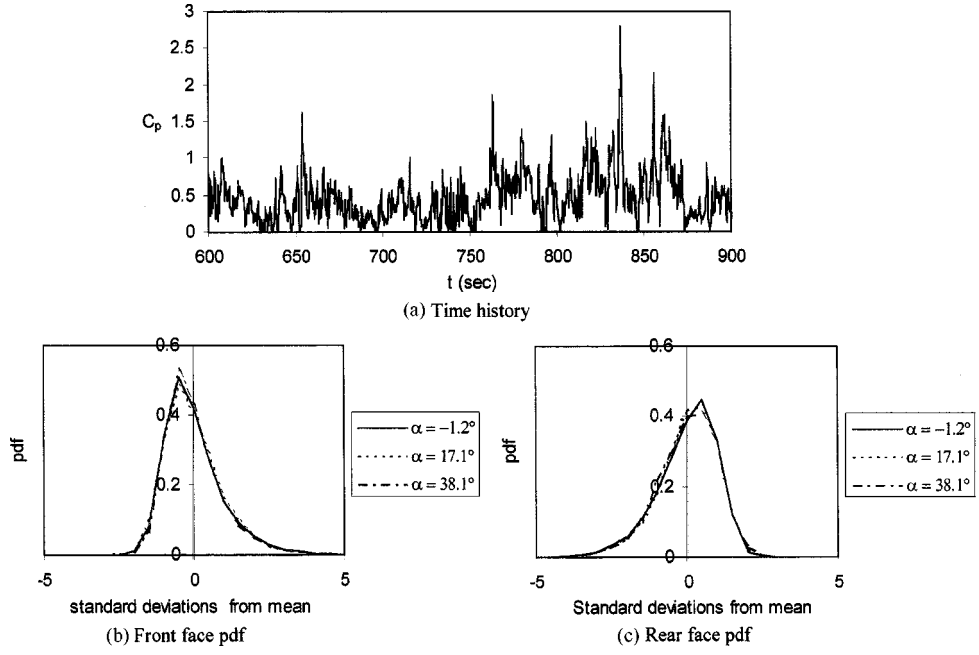

Fig. 6 Pressure coefficient time history and probability density functions at $x / h = 4.5$

represent gust factors (defined as (extreme value - mean) / standard deviation) of around 5 to 6 on the front face and 4.5 to 5.5 on the rear face i.e., well in excess of the values of around 3 to 3.5 that would be expected for a Gaussian process. It is worth noting at this point that this very simple method of extreme value analysis was used rather than the usual more sophisticated methods for a number of reasons, the main one being that a normal extreme value analysis would require around 10 to 20 identical runs in stationary conditions, which is almost impossible in the full scale situation. Also Hoxey *et al.* (1996) show that the use of extreme value analysis using full scale data is fraught with difficulties because the use of data that is not absolutely stationary can result in significant errors. The calculation of extreme values of pressure coefficient will be considered further in section 7.

Fig. 8 shows the autocorrelation functions of pressure coefficient at $x / h = 4.5$ on the front and rear faces. These are defined as

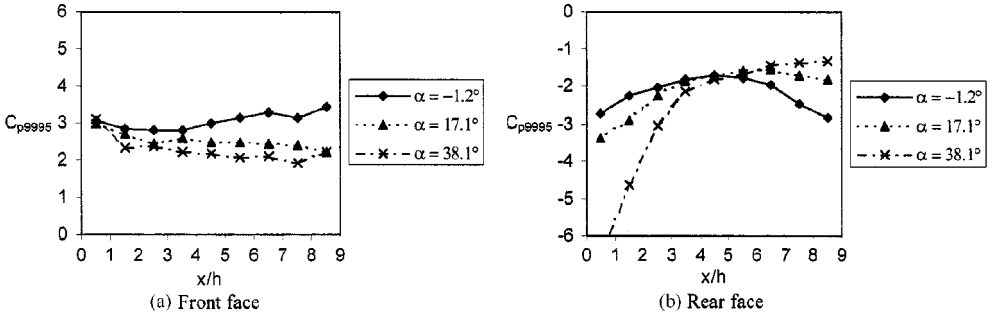

Fig. 7 Extreme values of pressure coefficients

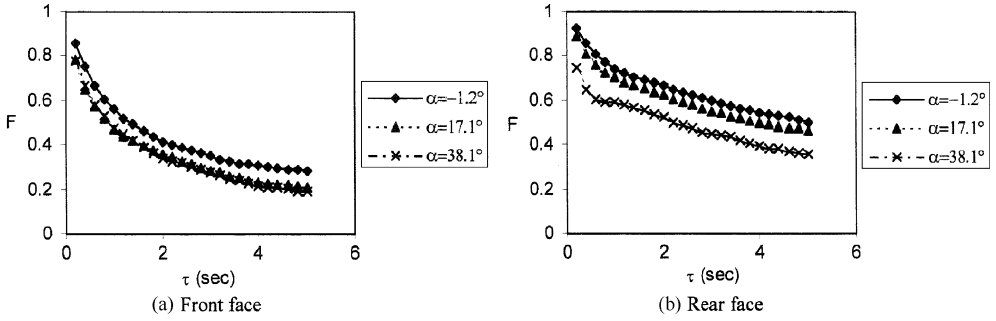

Fig. 8 Pressure coefficient autocorrelation functions at $x/h = 4.5$

$$F = \frac{\overline{C_p(t)C_p(t+\tau)}}{\sigma_{cp}^2} \tag{2}$$

$C_p(t)$ is the instantaneous pressure coefficient at time t, τ is a lag time and the overbar indicates time averaging over t. These functions fall off with lag as expected. The important thing to note from these results is that the autocorrelations on the rear face are rather higher than on the front face. The results are similar at all points along the wall. Similar trends can be observed in the cross correlation functions of Fig. 9. For pressure coefficients measured at positions i and j the cross correlation functions are defined in a similar manner to the autocorrelation functions as

$$C = \frac{\overline{C_{pi}(t)C_{pj}(t+\tau)}}{\sigma_{cpi}\sigma_{cpj}} \tag{3}$$

Fig. 9 shows the cross - correlation functions of the front face panels with panel 5 at $x/h = 4.5$ and the cross- correlation functions of the rear face panels with panel 14, again at $x/h = 4.5$. Together these correlation plots suggest that the general flow structure is more coherent on the rear face than on the front face. Fig. 10 shows the correlation of front and rear face pressure coefficients with the longitudinal velocity (i.e., with the velocity replacing one of the pressure coefficients in the above equation. As would be expected positive correlations occur on the front face and negative correlations on the rear face. It can be seen that on the front face the magnitude of these correlations are greatest at low values of x/h (i.e., at the end of the wall nearest the anemometer). On the rear face the magnitudes are more nearly constant. The correlation coefficients for the pressures with the

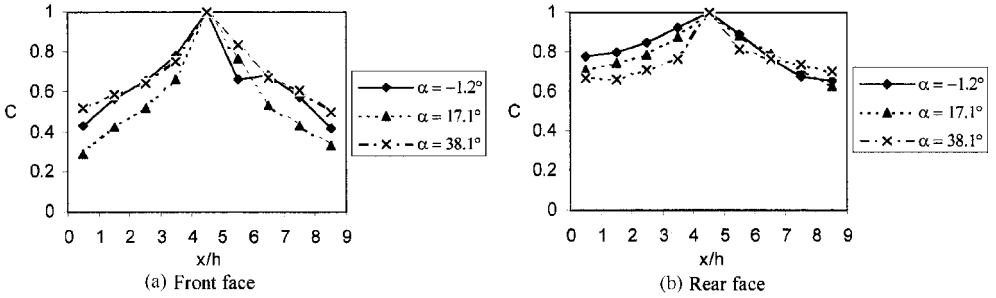

Fig. 9 Pressure coefficient cross-correlation functions at $x/h = 4.5$

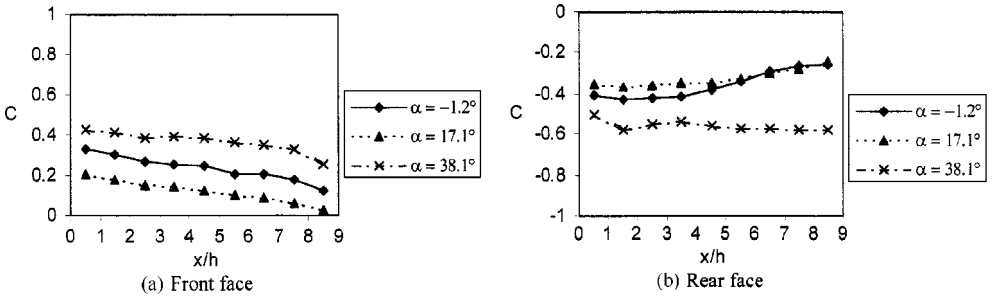

Fig. 10 Pressure coefficient cross-correlations with steamwise velocity

other velocity components is much smaller (nearly always less than 0.1). It is further of interest to note that the magnitudes of the correlations are highest at the higher wind angles, which may be due to a flow along the face of the wall leading to increased correlation levels.

Fig. 11 shows pressure coefficient spectra S_{cp} at $x/h = 4.5$ on the front and the rear faces for the highest and the lowest wind angles. The spectra are plotted in the form of an admittance X_{cp} given by

$$X_{cp} = \frac{S_{cp}/\sigma_{cp}^2}{S_u/\sigma_u^2} \tag{4}$$

This type of presentation allows the similarity or otherwise of the spectra to the upstream velocity spectra to be seen clearly. Spectra at the the other points on the front and rear faces were similar to those shown. For both wind angles the front face admittances are less than unity at low frequencies and greater than one at the higher frequencies. This may reflect both a small degree of aliasing in the pressure coefficient data, and also the fact that the velocity was not measured on the stagnation streamline, but someway above it. At the lower, normal wind angle the rear face admittances are close to one at all frequencies but a slight fall below one can be discerned at the higher frequencies, suggesting some attenuation of the effects of upstream turbulence by the separated wake. For the 38.1° case the situation on the rear face is more complex, with a dip in the admittance values in the mid-frequency range. At the higher wind angle there is a suggestion of a low frequency peak at around 0.02 Hz on both the front and the rear faces. In general these results suggest that a greater proportion of the energy in the fluctuations on the rear of the wall is in the low frequency range than on the front of the wall.

The spectra presented in Fig. 11 are effectively calculated from the Fourier transform of the auto-correlation of pressure coefficients. It is also possible to calculate the cross spectrum from a Fourier transform of the cross correlation function for pressure coefficients at positions i and j (S_{cpij}). This

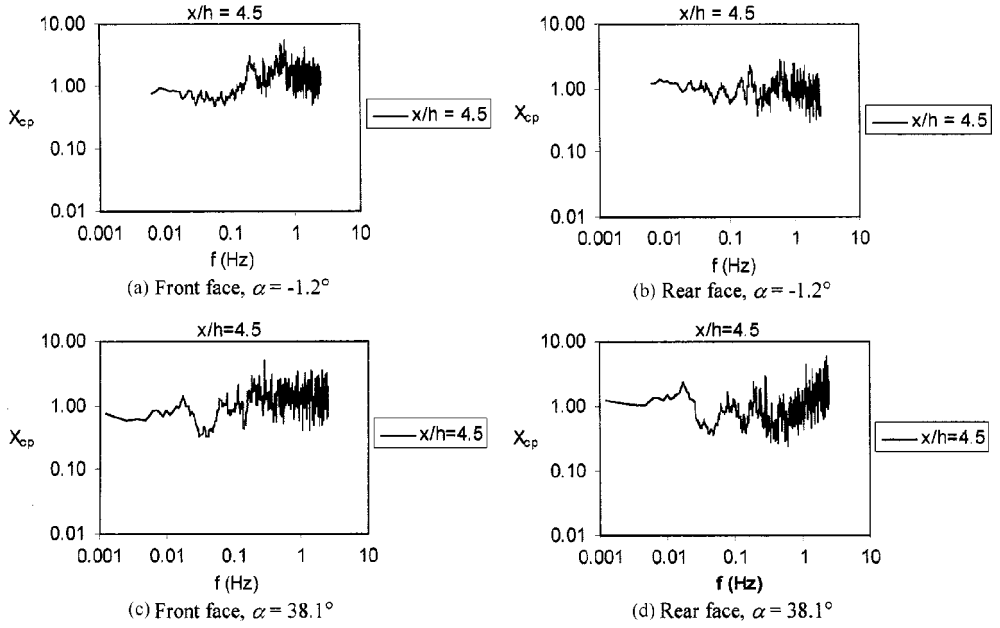

Fig. 11 Pressure coefficient admittances

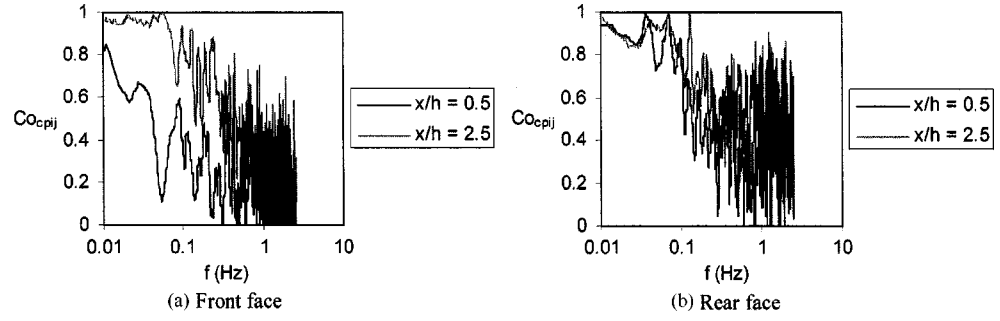

Fig. 12 Normalised pressure coefficient coherence with pressure coefficientat $x/h = 4.5$, $\alpha = -1.2^{o}$

parameter, which is in general complex, indicates the correlation of the data across the frequency range. Fig. 12 shows typical values of the coherence, a non-dimensional representation of the cross spectrum given by

$$Co_{cpij} = \frac{|S_{cpij}|}{\sqrt{S_{cpi}S_{cpj}}} \tag{5}$$

Values of the coherence are presented for the pressure coefficient measurements at $x/h = 0.5$ and 2.5 with those at $x/h = 4.5$ for the lowest wind angle only, although these are typical of all the other data. It can be seen however that the coherence falls with frequency and, unsurprisingly, the nearer the pressure measuring positions, the higher the magnitude. Again there can be seen to be generally higher values on the rear face than on the front face. There is some indication of a rise in this parameter at high frequencies, which is obscured by noise. This point will be taken up in section 6 below.

Now Newberry *et al.* (1973) showed that for a high rise structure, experimental values of

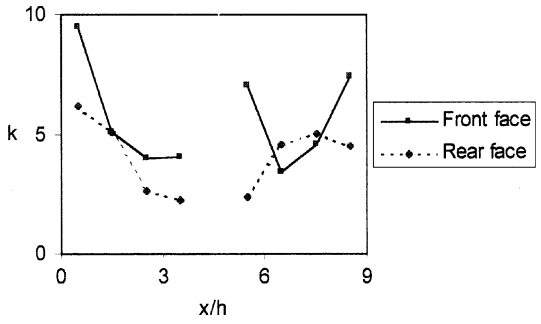

Fig. 13 Distribution of k values from normalised co-spectra for $\alpha = -1.2^o$

Table 2 k values from normalised co-spectra curve fits

Direction	-1.2°	17.1°	38.1°
Front face average k	5.64	13.65	2.35
Rear face average k	4.06	3.65	2.84

coherence could be represented by

$$Co_{cpij} = e^{-kfy/U} \tag{6}$$

where y is the separation of the pressure tappings and k is a constant. Values of the parameter k were calculated for the wall data. The precise values that were obtained were very sensitive to the precise nature of the curve fitting technique that was used, and there are large error bounds (around $\pm$50%). This being said, Fig. 13 shows typical k values for the lowest wind angle for values of the coherence formed with the pressure coefficient measured at $x/h = 4.5$. It can be seen that in general the values of k increase with distance from the tapping at $x/h = 4.5$. The values of k are higher on the front face than on the rear, which is consistent with lower correlations on the front face. Values range from about 2 to 10. Table 2 shows the average values of k for all the data that was considered. The average rear face value is constant at around 3 to 4, whilst the front face values vary from 2.35 to 13.65 with the greatest values being at the middle wind angle. The low front face value at 38.1° suggests an along wall flow that causes an increase in correlations along the wall, which is consistent with the velocity correlations of Fig. 10.

Thus in summary conventional statistical analysis of the unsteady wind loading data suggests the following.

a) The intermittent peaks in pressure coefficient, at least on the front wall, are related to similar peaks in the upstream wind field.
b) Very high suctions can develop in the wake of the wall at high angles of incidence.
c) The flow over the rear of the wall is temporally and spatially more coherent than over the front of the wall, with some suggestion of low frequency oscillations when the wind is at an angle of incidence.

4. Conditional sampling

It is clear from the above that the extreme loads on the wall are to some extent due to discrete events, and thus it is appropriate to use the technique of conditional sampling to investigate this

further. Such procedures have been adopted in the past by Letchford and Mehta (1993) and Kareem (1997) amongst others. A technique similar to those used by these authors has been adopted here. Firstly discrete events were identified at a particular panel. These were defined as when the pressure coefficient exceeded the 99th percentile value. "Events" less than two seconds apart were taken to be one event with the peak value being given by the greater peak. During each event the time at which the maximum value occurred was noted. An average was then formed of the pressure coefficients for all such events at a particular "trigger" for all panels C_{pcs}, over a period of 2 seconds either side of the maximum. Four particular trigger positions were used - extreme events at panels 1 and 5 on the front face ($x / h = 0.5$ and 4.5) and panels 10 and 14 on the rear face ($x / h = 0.5$ and 4.5) i.e., at the end and the centre of the front and rear faces. This process should thus reveal the spatial and temporal extent of the discrete extreme events.

Figs. 14 and 15 show typical results of the analysis at $x / h = 0.5$, for both the smallest and the greatest wind angles. The front face results (Figs. 14a,b and 15a,b) show that on average such events last a second or so either side of the maximum value, and spatially extend over only a short distance i.e., they can only be discerned at pressure taps close to the trigger. Such events can also be discerned, just, on the rear face at $x / h = 0.5$, immediately behind the trigger location, but not at any other position on that face. With the event at $x / h = 0.5$ on the rear face as the trigger (Figs. 14c,d, Figs. 15c,d), the event lasts rather longer (up to two seconds either side of the peak), but is again of a limited spatial extent. Such events can be observed at $x / h = 0.5$ on the front of the wall for the lowest wind angle, but at the highest wind angle the effects of these events are confined to the rear of the wall. For events at $x / h = 0.5$ on both the front and rear faces a detailed inspection of the data of Figs. 14 and 15 show that the actual events seem to take place during a period of relatively high average pressure coefficients, i.e., the short term peak events are superimposed upon longer period

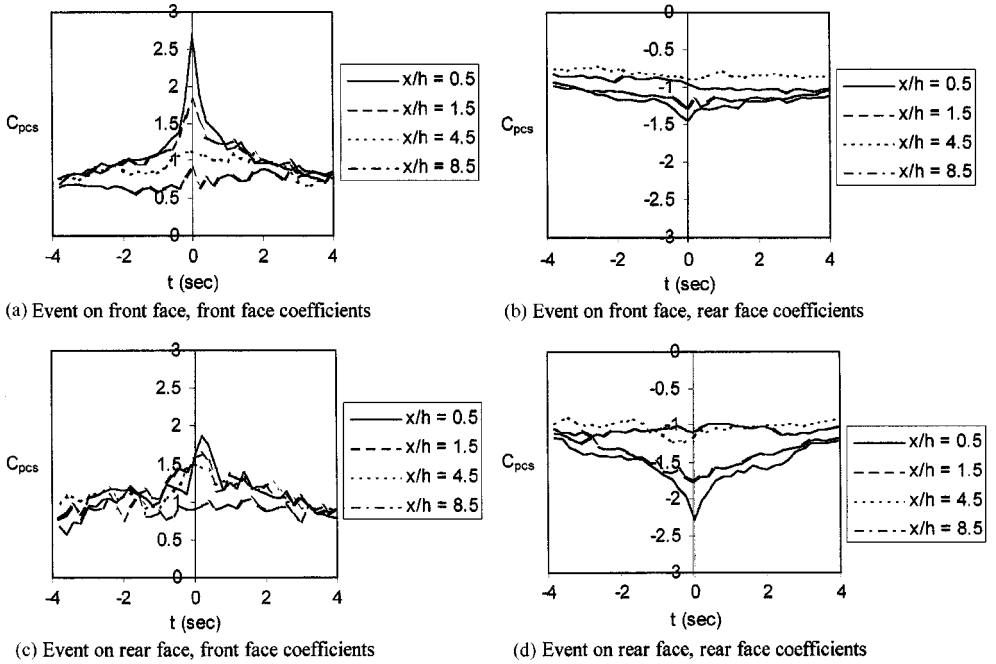

Fig. 14 Conditional sampling at front and rear wall events at $x / h = 0.5$, $\alpha = -1.2^{o}$

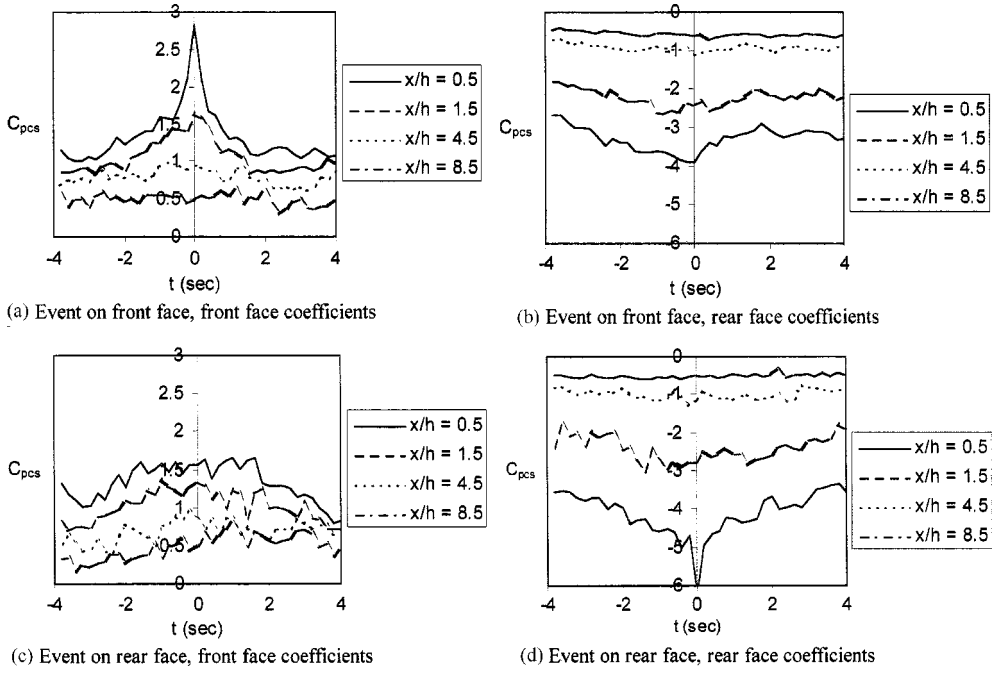

(a) Event on front face, front face coefficients

(b) Event on front face, rear face coefficients

(c) Event on rear face, front face coefficients

(d) Event on rear face, rear face coefficients

Fig. 15 Conditional sampling at front and rear wall events at $x/h = 0.5$, $\alpha = 38.1^{o}$

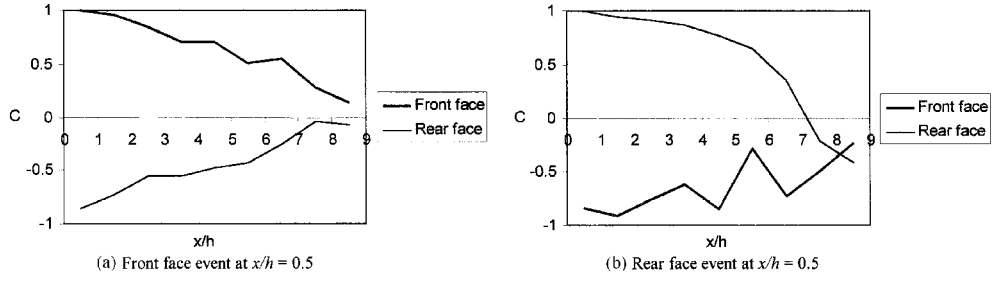

(a) Front face event at $x/h = 0.5$

(b) Rear face event at $x/h = 0.5$

Fig. 16 Conditionally sampled pressure coefficient cross-correlation with coefficient at trigger location for $\alpha = -1.2^{o}$

peaks. There is no consistent, discernible time lag between the results at the trigger position and the results at other locations.

The streamwise velocity time histories were also conditionally sampled around the trigger events for the conditions of Figs. 14 and 15. No short term peaks were found. This is not surprising since the anemometer mast was some distance away from the pressure measuring positions, and even if the short term pressure peaks are directly related to short term gusts, there is unlikely to be a one to one correspondence between events measured at the anemometer and those measured at the pressure taps because the travel time between the locations is of the same order or greater than the event duration. Also note that the correlations between upstream velocity and pressure coefficient shown in Fig. 10 are relatively low. This being said however the conditionally sampled velocity values around peak pressure events are significantly above the mean values thus indicating that the peaks occur around the peak of long duration fluctuations in wind speed.

Table 3 Percentage of events at each trigger

Trigger	-1.2°	17.1°	38.1°
x/h = 0.5 on front only	21.2	16.6	23.8
x/h = 4.5 on front only	19.6	20.0	26.1
x/h = 0.5 on rear only	1.5	6.7	7.1
x/h = 4.5 on rear only	4.5	3.3	11.9
2 triggers	33.3	36.7	14.2
3 or 4 triggers	19.7	16.6	16.6

Table 4 Length of event at each trigger T

Trigger	-1.2°	17.1°	38.1°
x/h = 0.5 on front	2.29	2.63	2.01
x/h = 4.5 on front	2.63	2.51	2.23
x/h = 0.5 on rear	4.47	7.14	4.08
x/h = 4.5 on rear	3.08	5.80	2.51
Total velocity	2.98	2.99	-

Fig. 16 shows the cross correlation functions of conditionally sampled pressures for the events shown in Fig. 14. These curves show a rather greater level of correlation than the graphical plots of Fig. 14 would lead one to expect, but emphasise what has already been said, with the region of good correlation for rear face events being greater than for front face events.

Table 3 presents some statistics of the events at the four trigger locations. For each wind angle a breakdown of extreme events is shown, in terms of whether these events can be discerned at only one trigger location or at a number of locations. It can be seen that events on the front face are far more likely to occur in isolation than events on the rear face, which usually occur together with events on the front face. About half of the events can be detected at more than one trigger location.

Table 4 shows the period of the events measured at each trigger for each wind angle. The period (T) is defined as the total time for which the 99th percentile was exceeded divided by the number of observed events, non-dimensionalised by multiplying by U and dividing by h. It can be seen that the events on the rear face last for a dimensionless time of about 4.5 on average, whilst events on the front face last for a dimensionless period of 2.4 on average, which is in agreement with the trend observed in Figs. 14 and 15. A similar analysis was carried out for similar events in the upstream total velocity record. The average length of event in this case was found to be around 3. This lends further, if inconclusive, support to the hypothesis that the events on the front face are associated particularly with extreme events in the upstream wind field.

Thus, in summary, the conditional sampling of extreme events indicate that peak events on the front face are of a shorter duration than on the rear face, and are much more likely to occur in isolation. There is evidence to suggest that the front face events are caused by short duration peaks in the upstream velocity field, that occur near the peak of longer term fluctuations. On the rear face it may be hypothesised that the extreme events occur when these upstream events correspond with the peaks of longer duration wake fluctuations.

5. Application of the technique of proper orthogonal decomposition

The technique of proper orthogonal decomposition (POD) has come to be applied to a number of

wind engineering problems in recent years. A good description of the fundamentals of the method are given in Holmes (1990) and Tamura *et al.* (1999), who discuss the physics behind this approach in some detail. Essentially this approach assumes that the fluctuating pressure field can be expressed as a multiple of spatial and temporal functions as follows.

$$C_p(t) = P_1T_1 + P_2T_2 + \ldots\ldots + P_iT_i \tag{7}$$

In this equation $C_p(t)$ is the fluctuating pressure coefficient, P_i are spatial functions and T_i are temporal functions. Making the assumptions that the spatial functions are orthogonal and the temporal functions are uncorrelated, then the spatial functions can be shown to be the eigenvectors of the pressure coefficient covariance matrix, and the eigenvalues of that matrix represent the mean square of the temporal functions. The sum of the eigenvalues is equal to the sum of the variances of the fluctuating pressure coefficients, and thus represents the total fluctuating energy. It is also possible to write the following formulae for the relationship between the pressure coefficient spectrum S_{cp} and the mode spectra S_{Ti}, and the pressure coefficient standard deviation σ_{cp} and the eigenvalues of the covariance matrix.

$$S_{cp} = P_1^2S_{T1} + P_2^2S_{T2} + \ldots\ldots + P_i^2S_{Ti} \tag{8}$$

$$\sigma_{cp}^2 = P_1^2\overline{T_1^2} + P_2^2\overline{T_2^2} + \ldots\ldots + P_i^2\overline{T_i^2} \tag{9}$$

The utility of this method is that it is usually found that nearly all of the fluctuating energy is contained within the largest few modes, and thus the complete fluctuating pressure field can be represented by a relatively small number of functions.

A POD analysis of the almost normal wind data ($\alpha = -1.2^o$) has already been carried out by the author and is presented in Baker (2000), as one of a number of such analyses for a variety of structures. The purpose of that analysis was to attempt to identify particular modes with specific flow mechanisms. This was achieved through a comparison of the measured mode shapes with those predicted by quasi-steady theory, and through a comparison of the modal spectra with the spectra of the upstream components of velocity. For the wall with a normal wind the first mode was shown to be associated with the longitudinal velocity fluctuations, and the third mode with lateral velocity fluctuations, although in neither case was the association perfect. No particular physical mechanism was suggested that could be associated with the second mode, and Baker (2000) cautions against making any attempt at similar identifications for the less energetic higher modes, because of experimental variability and error, and discretisation errors.

In what follows therefore we will consider the variation of mode shapes with wind angle, concentrating on the first three modes. An analysis of the eigenvalues showed that for all wind directions the large majority of the fluctuating energy within the flow is contained in the first three or four modes, although there is no reason why there should be any identity between the different modes for the different wind angles. Fig. 17 shows the mode shapes on the wall for the three wind angles. The mode shapes at an angle of 17.1^o are similar in form to those for the near normal wind angle of -1.2^o (at least on the front face) and if the latter can be assumed to be due to certain physical mechanisms as outlined above, then presumably the same is the case for the former. At a wind angle of 38.1^o however, the mode shapes are rather different, particularly on the rear face. For this wind angle the only place where the eigenvectors for mode 3 differ greatly from zero is near the “leading edge” on the rear of the wall. This suggests that, for this angle, this mode is associated

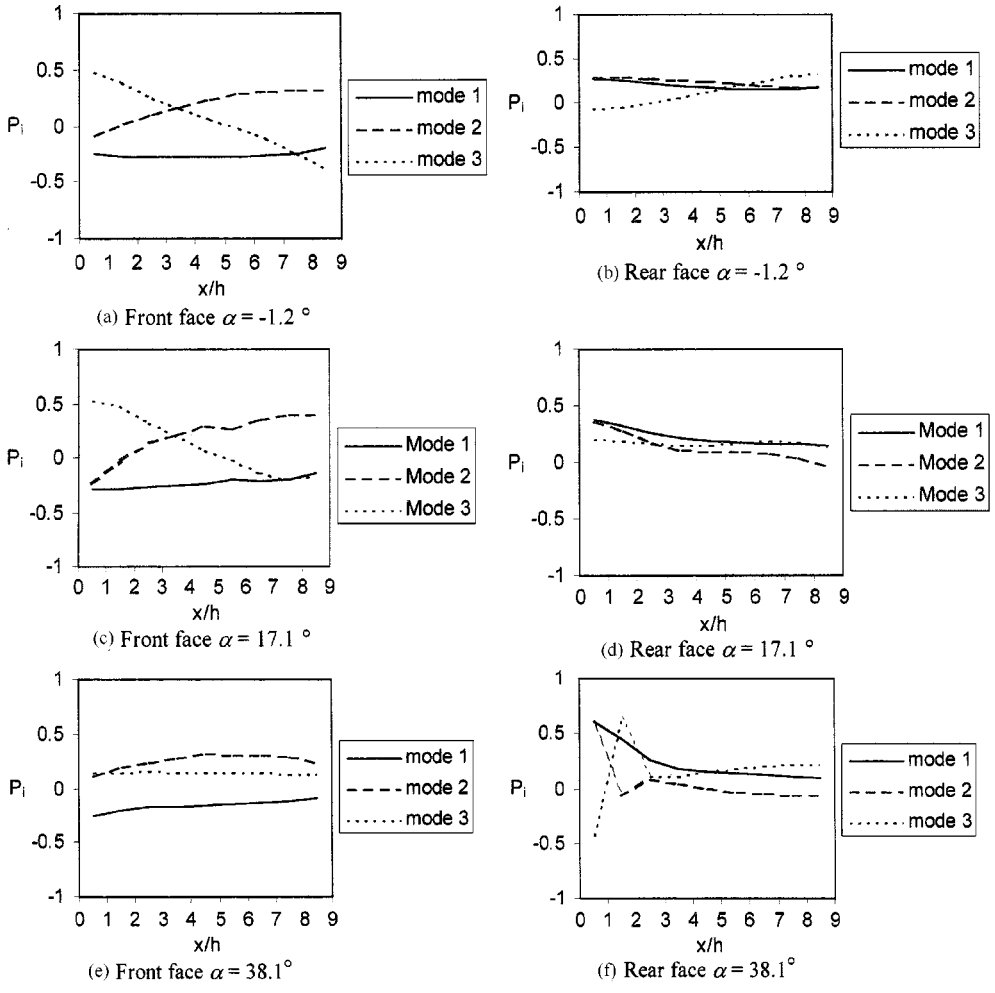

Fig. 17 Eigenvectors from POD analysis

with a separation in the lee of the wall at the leading edge. This is not to say that the lateral quasi-steady effects associated with this mode at the lower wind angles are not still significant, but may be represented by a mode other than the third.

Fig. 18 shows the modal spectra, again plotted in an admittance form given by

$$X_{Ti} = \frac{S_{Ti}/\overline{T_i^2}}{S_u/\sigma_u^2} \tag{10}$$

This format again allows a direct comparison of the modal spectra with the oncoming velocity spectra. At the lower wind angle the admittances for modes 1 and 3 do not vary greatly from a value of 1.0 except at the higher frequencies. Baker (2000) shows that this is consistent with these modes being primarily caused by longitudinal and lateral upstream turbulence fluctuations. Mode 2 however shows more energy at higher frequencies than at low frequencies, with a peak at 0.5 Hz, which corresponds to a Strouhal number based on U and h of around 0.1. At $\alpha = 17.1^{o}$ the mode 1

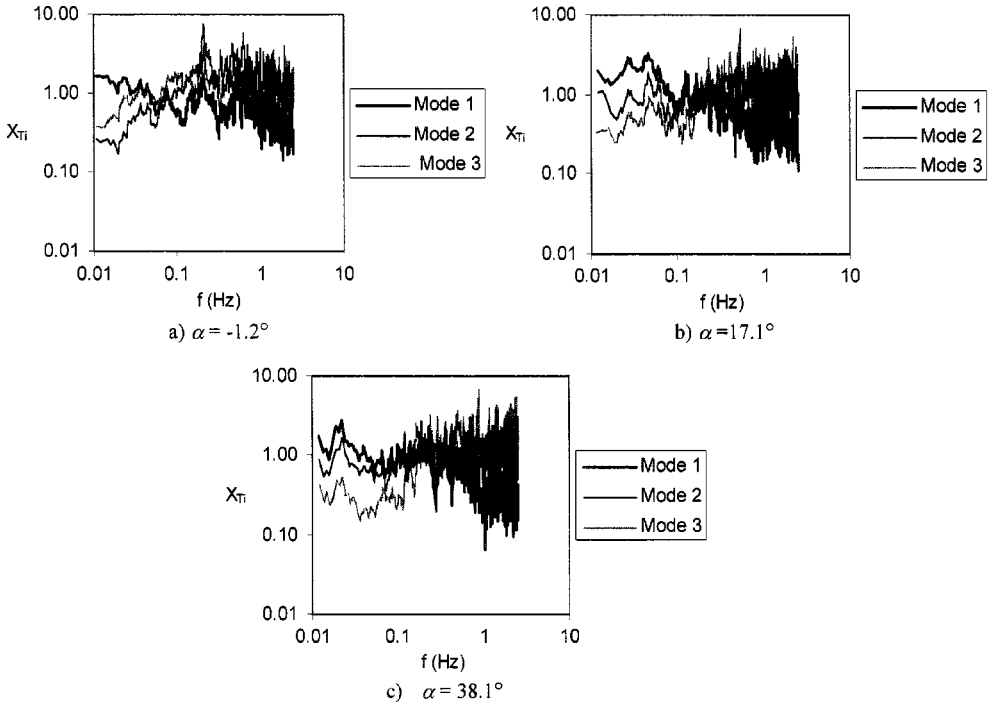

Fig. 18 Mode admittances

admittance falls off more rapidly at the higher frequencies, the mode 2 admittance is close to unity, and the mode 3 admittance shows a larger proportion of energy in the high frequency range. At $\alpha = 38.1^{o}$ these trends are also apparent. From these results one can thus tentatively hypothesise that, at the lower wind angle mode 2 is primarily associated with a wake fluctuation, since this is consistent with the frequency range in which most of the energy is found. As the wind angle increases the nature of this fluctuation inevitably changes somewhat and becomes localised at the leading edge in the lee of the wall, and there is a change in order of the modes, so that it becomes primarily associated with mode 3. This is confirmed to a degree by the plots of Fig. 19, which show the contribution of each mode to the total fluctuating energy at each measurement point. The results at $\alpha = -1.2^{o}$ show a considerable asymmetry, but do confirm that mode 2 is of most significance on the rear of the wall and at the ends of the front of the wall - the places where any pressure fluctuations due to large scale wake unsteadiness would be expected to be of most importance. At the highest wind angle, $\alpha = 38.1^{o}$, mode 3 is only significant on the rear of the wall, being of greatest importance at a point near the leading edge ($x / h = 1.5$). However this argument is very speculative and the main point to emerge from this study is that it is very difficult to assign physical meanings to POD modes, except in the simplest of geometries.

Taken together with the results of Baker (2000) these results suggest that we can further conclude that the unsteady pressure fluctuations, at least at lower wind angles are to a significant degree caused by quasi-steady fluctuations in the longitudinal and lateral velocities in the approach flow but that a contribution due to wake unsteadiness can also be inferred. At the higher wind angles, the vigorous separation in the lee of the wall results in large fluctuations around the leading edge.

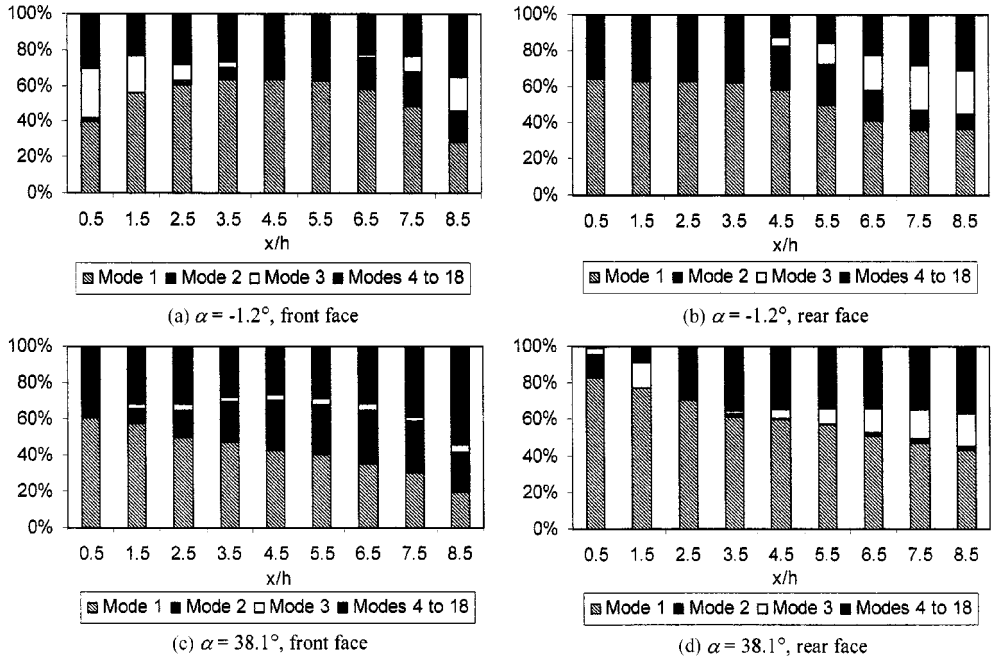

Fig. 19 Breakdown of variance by mode for each measurement position

6. Wavelet analysis

In a similar fashion to POD, wavelet analysis has become popular in the analysis of wind engineering datasets in recent years. Essentially wavelet analysis enables the variation of power within a fluctuating signal to be resolved into a series of fluctuating time series each representing the power at a particular scale or period (which corresponds to a particular Fourier frequency). As such, wavelet analysis enables something equivalent to short period power spectra to be derived. It is thus an ideal tool for the investigation of the power content at different frequencies for non-stationary signals. A good description of the use of wavelet analysis is given in Torrence and Compo (1998), and its applications to wind engineering are discussed in Gurley and Kareem (1999). Essentially the technique is as follows. The time series of the pressure coefficient, measured at N intervals separated by a time of δt, $C_p(t)$ is convoluted with a wavelet function $\psi(\eta)$ to produce the wavelet transform $w_{cp}(s, n)$. This can be written as

$$w_{cp}(s, n) = \sum_{n' = 0}^{N-1} C_p(n'\delta t)\psi^*\left[\frac{(n' - n)\delta t}{s}\right] \tag{11}$$

In the above equation s is the wavelet scale or period. The parameters n and n' define the position in the time series. This procedure is carried out for a number of values of s to produce time series of the wavelet transform for each value of s. A number of different wavelet functions are in common use. In what follows we will use the Morlet wavelet which consists of a plane wave modulated by a Gaussian. This is given by

$$\psi_0(\eta) = \pi^{-1/4} e^{i\omega_0\eta} e^{-\eta^2/2} \tag{12}$$

where ω_0 is a non-dimensional frequency parameter. The wavelet function can be written in a normalised form as follows

$$\psi(\eta) = \left(\frac{\delta t}{s}\right)^{1/2} \psi_0(\eta) \tag{13}$$

In practice it is easier to carry out the convolution in the frequency domain by multiplying together the Fourier transforms of the pressure coefficient time series and the wavelet function, and then taking the inverse transform. This method is simply set out in Torrence and Compo (1998). Finally the wavelet power spectrum can be calculated from

$$W_{cp}(s, n) = |w_{cp}(s, n)|^2 \tag{14}$$

Now the fact that the pressure coefficient time histories on the wall are heavily influenced by intermittent peaks makes them obvious candidates for a wavelet analysis. An analysis was thus carried out for pressure coefficient time series for the $\alpha = -1.2^o$ case, using a Morlet wavelet base with the parameter $\omega_0 = 6$. Twenty distinct scales or periods were used that ranged from 0.4 sec to 410 sec. For each time series this resulted in a set of 20 time series of the same length across the range of periods. Fig. 20 shows the mean wavelet spectra ($W_{cp}(s)$) obtained from finding the average of each of these time series. The results are shown in an admittance format defined as

$$X_{wcp} = \frac{W_{cp}(s)/\sigma_{cp}^2}{W_u(s)/\sigma_u^2} \tag{15}$$

where subscript u indicates the wavelet spectrum and standard deviation of the upstream mean velocity. The x axis is shown in terms of a Fourier frequency rather than a scale for ease of comparison with other spectra. For the Morlet wavelet this relationship is $f = \omega_0 / 2\pi s$. These plots are thus effectively analogous to the admittances for the ordinary power spectra (Fig. 11). The front face admittances increase at high frequency and are consistent with Fig. 11, whilst the rear face admittances decrease, a trend which is not strongly observed in Fig. 11.

A conditional sampling was then carried out on the results. For the peak events identified in the conditional sampling of section 4, at $x/h = 4.5$ on the front and rear face, the average wavelet power spectrum at each scale or period was calculated at each measurement position on the front and rear face, for one second either side of the peak event. This thus represents a measurement of the wavelet energy distribution with frequency at peak events. Fig. 21 shows this parameter plotted

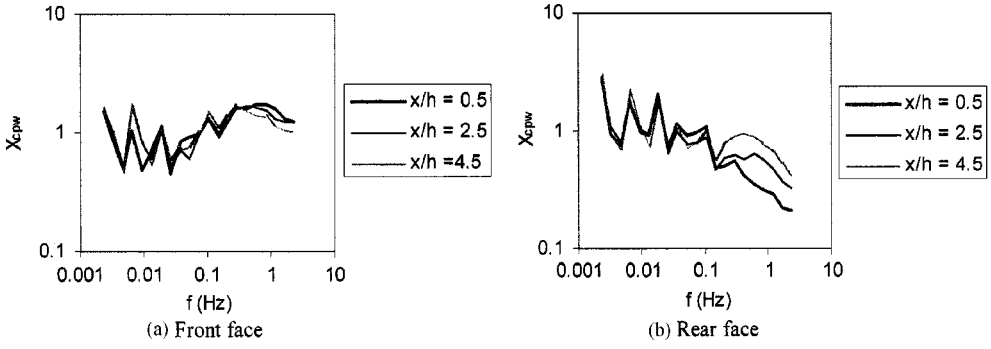

Fig. 20 Wavelet spectra admittances at $\alpha = -1.2^o$

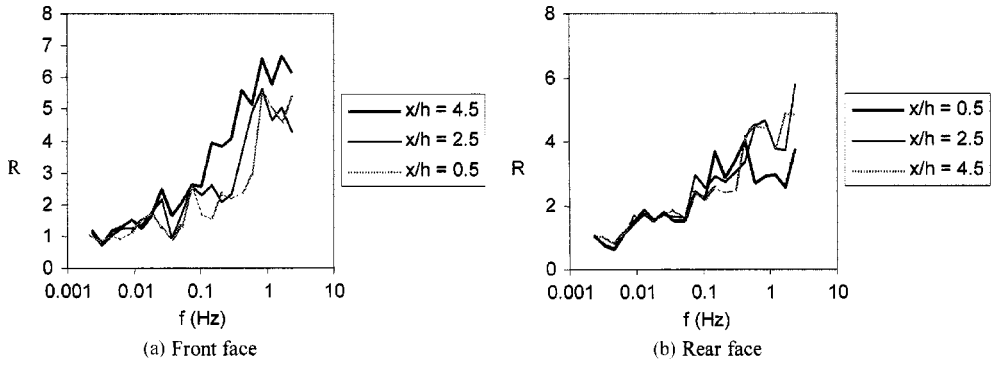

(a) Front face (b) Rear face

Fig. 21 Ratio of extreme to mean wavelet power for event at $x/h = 4.5$ with $\alpha = -1.2^{o}$

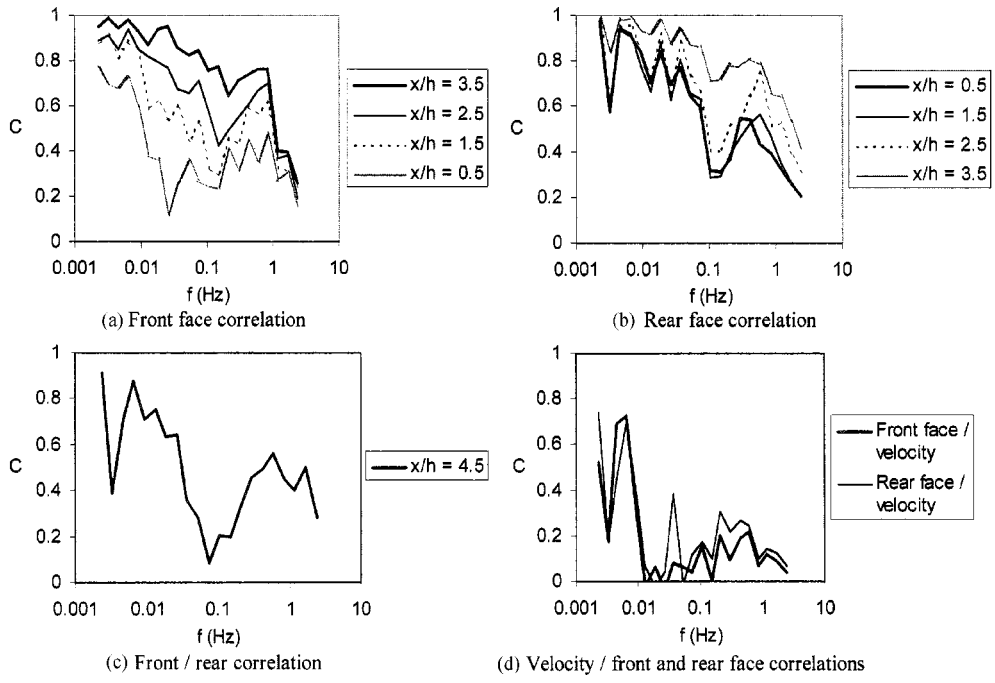

(a) Front face correlation (b) Rear face correlation

(c) Front / rear correlation (d) Velocity / front and rear face correlations

Fig. 22 Wavelet correlation by scale for $\alpha = -1.2^{o}$ with event at $x/h = 4.5$

as a ratio with the average wavelet power spectrum (R). It can be seen that at the peak events there is a very considerable enhancement of energy at higher frequencies. This is particularly noticeable at frequencies above about 0.1 Hz, and this effect is stronger on the front face than on the rear. A similar enhancement of energy at small scales in peak events was noticed by Jordon *et al.* (1997) in their study of wavelet intermittency and energy associated with peak events.

The wavelet analysis also enables the correlations between the wavelet energy of the different pressure coefficient time series to be investigated for each wavelet period. Fig. 22(a,b) shows the cross correlation functions of the wavelet energy of the pressure coefficient time histories, as a function of the equivalent Fourier frequency, for the front and rear face of the wall at $x/h = 4.5$. It can be seen that at the lowest frequencies there is a high degree of correlation, which is probably

due to the passage of large scale gusts over the wall, and is consistent with the results of Jordon *et al.* (1999). This correlation falls off as the frequency increases as would be expected. However it is interesting to note that the correlation increases at frequencies of around 0.5 Hz. This occurs for correlations on both the front and rear faces. Fig. 22c shows that this also occurs for the correlations between the wavelet energies of the pressure coefficients on the two faces. This raises the possibility that these relatively high correlations at high frequencies are caused by small scale coherent structures within the atmosphere passing over the wall. Fig. 22d shows the correlations of the wavelet power of the pressure coefficients at $x / h = 4.5$ on the front and rear faces with the wavelet energy of the upstream velocities. It can be seen that the correlations are only significant at low frequencies, due to the distance between the velocity and the pressure measuring positions effectively reducing the correlations at small scale. There is however a slight indication of increased correlation at higher frequencies of around 0.5 Hz.

7. Discussion

In this section we consider the implications of the results presented in sections 3 to 6. Section 7.1 presents a description of the unsteady flow field around the wall, based on the experimental results. Since it is apparent that the unsteady flows are influenced to a large extent by the nature of the upstream turbulence, section 7.2 goes on to consider the quasi-steady hypothesis and its adequacy for predicting the fluctuating surface pressures. Section 7.3 then discusses methods of describing the extreme values of the load and section 7.4 then goes on to consider the implications of the results for a number of aspects of the codification of wind loading data and in particular the specification of extreme events.

7.1. The flow around the wall

It is apparent from the results of earlier sections that the unsteady wind loading on the wall is to a large extent influenced by the turbulence in the oncoming boundary layer, particularly on the windward face. Visually the time histories of velocities and pressure coefficients are similar, with discrete, very short period peaks (Figs. 2 and 6). In more quantitative terms the probability distributions of pressure coefficient exhibit a skewness that is similar to that of the upstream dynamic head; the admittances of the spectral density functions are close to unity over a large frequency range (Fig. 11); the dimensionless duration of the extreme peaks is similar to that of the extreme peaks on the front face of the wall (Table 4); and finally POD identifies modes that can be associated, albeit imperfectly, with longitudinal and lateral upstream turbulence (Fig. 17) and these modes account for around 75% of the total variance in the fluctuations. Thus in the first instance the unsteady flow around the wall can be considered to simply reflect the upstream turbulence, both in a general manner, and at extreme events.

This point being made however there is also a contribution to the overall flow field from the unsteady flow in the wall wake, although this is perhaps not as strong as would be expected. The auto-and cross correlation functions of pressure coefficient show a greater correlation on the rear of the wall than on the front, suggesting some large scale flow structure (Figs. 8 and 9); the pressure coefficient admittances show a shift in energy to the lower frequency ranges (Fig. 11); the extreme events on the rear wall last significantly longer than those on the front wall and are somewhat better correlated along the length of the wall (Table 4 and Figs. 14 and 15); and some of the POD modes

can be plausibly associated with the effects of wake unsteadiness. All these effects are most obvious for the near normal wind direction, and with non-normal wind directions are somewhat complicated by other effects - in particular a strong unsteadiness on the rear of the wall near the leading edge. However in general it does seem that some of the pressure coefficient fluctuations can be associated with a large scale, broad banded wake structure.

Now if the pressure coefficient fluctuations follow the upstream velocity fluctuations, the nature of the latter are of some interest. It is here that the experimental data that has been used is not entirely adequate, since the only velocity data are from a single reference anemometer at wall height. It is thus not possible to infer the structure of the wind from this data. However an inference can be made from the pressure coefficients measured on the front face of the wall, which can, in a rather crude way, be regarded as "surrogate" anemometers. It is in this respect that the wavelet analysis has proved to be significantly useful (Fig. 22). This analysis showed that there is a strong correlation between the wavelet energy of the pressure coefficients at low fequencies (around 0.01 Hz) which must be associated with the passage of large gusts over the structure, that affect all the pressure tappings. At frequencies of around 0.1 Hz the pressure coefficient wavelet energy correlations fall markedly, and only achieve high values for pressure tappings that are close to each other. However at frequencies of around 0.5 to 1 Hz the correlations increase. This effect can be seen on the front and rear faces of the wall, and for correlations between the two faces. It suggests the existence of small scale structures within the wind with a duration of around this period, and of a lateral length scale of around the length of the wall. This existence of two scales in the oncoming wind is also suggested by the conditional sampling of extreme events - these seem to be associated with the superposition of short period events (1 to 2 seconds) on a longer term high level fluctuation (Figs. 14 and 15). However before this hypothesis of discrete turbulence scales in the atmospheric wind can be substantiated, more experimental data is required for simultaneous measurements of wind velocity at a number of locations.

7.2. The quasi-steady hypothesis

Essentially the quasi-steady hypothesis relates the surface pressure fluctuations to upstream velocity fluctuations. If $C_p(t)$ is the fluctuating pressure coefficient (based on fluctuating pressure and mean velocity) and C_p is the mean pressure coefficient, then this can be written

$$C_p(t) = C_p(\alpha, \beta)\frac{U(t)^2}{U^2} \tag{16}$$

where U is the mean reference velocity and $U(t)$ is the fluctuating reference velocity. $C_p(\alpha, \beta)$ is the mean pressure coefficient as a function of α (the instantaneous lateral wind angle) and β (the instantaneous vertical wind angle). It is usual to express both the presssure coefficient and the reference velocity in power law form as follows (e.g., Letchford *et al.* 1993).

$$C_p(t) = \left(C_p + \frac{dC_p}{d\alpha}\frac{v}{U} + \frac{dC_p}{d\beta}\frac{w}{U}\right)\left(1 + \frac{2u}{U} + \frac{u^2}{U^2} + \frac{v^2}{U^2} + \frac{w^2}{U^2}\right) \tag{17}$$

where u, v and w are the three unsteady velocity components in the longitudinal, lateral and vertical directions. Now for the case of the wall, the measurements reported in Hoxey *et al.* (1999) on a large cubic structure suggest that windward and leeward face vertical derivatives of pressure coefficient can be assumed to be zero. Assuming that this is also the case for the wall, Eq. (17) can

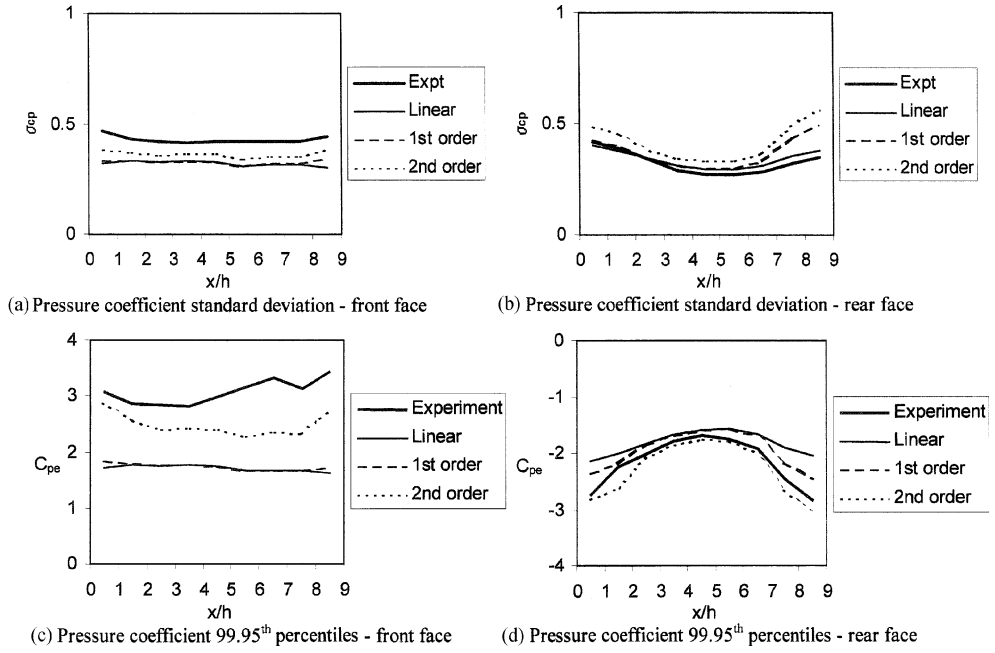

Fig. 23 Results of quasi-steady calculation for $\alpha = -1.2^o$

be expanded to a number of levels. The linear (zero order) expansion (ignoring everything except linear streamwise velocity terms) is

$$C_p(t) = C_p + 2C_p\frac{u}{U} \tag{18}$$

The first order expansion, which retains all the linear terms, is

$$C_p(t) = C_p + 2C_p\frac{u}{U} + \frac{dC_p}{d\alpha}\frac{v}{U} \tag{19}$$

The second order formulation which retains velocity squared terms and velocity products, is given by

$$C_p(t) = C_p + 2C_p\frac{u}{U} + \frac{dC_p}{d\alpha}\frac{v}{U} + C_p\left(\frac{u^2}{U^2} + \frac{v^2}{U^2} + \frac{w^2}{U^2}\right) + 2\frac{dC_p}{d\alpha}\frac{uv}{U^2} \tag{20}$$

The adequacy of the above expressions has been investigated for the wall data used in this investigation. Time series of the linear, first and second order fluctuating pressures have been calculated from the measured wind time series and the measured mean surface pressure coefficients and pressure coefficient derivatives. The results are shown, for the $\alpha = -1.2^o$ case, in Fig. 23, for the standard deviations and 99.95th percentiles of the calculated time series. It can be seen that for the front face the quasi-steady calculations approach the experimental values as the complexity of the quasi-steady calculations is increased. This is as expected. On the rear face the situation is more complex. All the quasi-steady calculations overpredict the standard deviation, and the second order calculations overpredict the extreme values. On the rear of the wall one would expect that the quasi-steady calculations would underpredict all the parameters, and the difference would be made up by unsteadiness due to the wake fluctuations, which one would expect to be independent of the

upstream turbulence. Since such wake fluctuations can be inferred to exist from the work presented earlier, one is forced to conclude that the wake fluctuations actually damp out the quasi-steady fluctuations in this region. This is of course contrary to what might be expected that such structure induced unsteadiness would add to the unsteadiness caused by the upstream flow.

7.3. Specification of extreme pressure coefficients

Cook (1990) lists four methods of specifying the extreme load on structures from full scale or experimental data. These are as follows

(a) Extreme value analysis
(b) Quantile level method
(c) Quasi-steady method
(d) Peak factor method

The first of these relies on having a significant number of datasets from which the maximum values can be extracted and fitted to an extreme value probability distribution. It has already been pointed out, based on the work of Hoxey *et al.* (1996), that the use of such a method with full scale data is likely to produce significant errors, since absolute stationarity cannot be guaranteed. It will not be considered further here. The second method is what has been used in this paper, in that extreme values corresponding to the 99.95th percentile level have been presented. This is a very rapid and convenient approach that give the level that is exceeded for 1.8 secs in one hour. It only makes use of a small amount of the data however, and unless the datasets extend over a considerable period, is prone to experimental scatter. The third approach is based on the quasi-steady assumption discussed in the last section, and in particular on Eq. (16). If subscript e refers to the extreme value then this equation becomes

$$C_{pe} = C_p \frac{U_e^2}{U^2} \tag{21}$$

The variation of the pressure coefficient with wind angle is usually ignored in this method. The peak factor method gives an analytical method for specifying the extreme values for processes which are Gaussian. It relates the extreme pressure coefficient to the mean coefficient C_p, the standard deviation of the coefficient σ_{cp} and a gust factor g_{cp} through the equation

$$C_{pe} = C_p + \sigma_{cp} g_{cp} \tag{22}$$

The gust factor is given by

$$g_{cp} = \sqrt{2\ln(\nu T_o)} + \frac{0.577}{\sqrt{2\ln(\nu T_o)}} \tag{23}$$

where T_o is the observation period, and the zero crossing rate ν is given by

$$\nu = \frac{\int_0^\infty f^2 S_{cp}\left(\frac{\sin(f\pi\tau_a)}{f\pi\tau_a}\right)^2 df}{\int_0^\infty S_{cp}\left(\frac{\sin(f\pi\tau_a)}{f\pi\tau_a}\right)^2 df} \tag{24}$$

with τ_a being the averaging time. The wall data allowed a comparison to be made between the

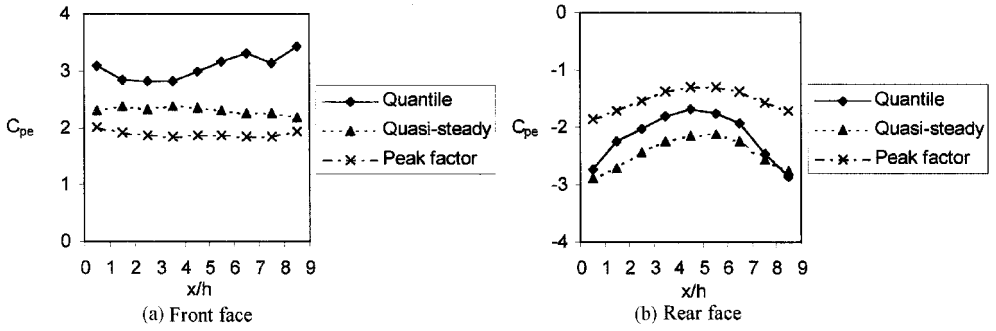

Fig. 24 Comparison of different methods of calculating extreme values of pressure coefficients for $\alpha = 1.2^o$

quantile level method, the quasi-steady method and the peak factor method. The results for $\alpha = -1.2^o$ are shown in Fig. 24. For consistency the value of U_e has been taken as the measured 99.95th percentile value, and the averaging time τ has been taken as 1.8s, and thus the three methods should be directly comparable. Assuming that the quantile method gives the true value, albeit one prone to experimental error, it can be seen that neither of the other methods predict the actual value of the extremes well. The quasi-steady method underpredicts on the front face and overpredicts on the rear face, which is consistent with the discussion of the last section. The peak factor method significantly underpredicts in all cases. An examination of the results of this method shows that the predicted values of the gust factor g_{cp} are between 3.07 and 3.15 on the front face and 2.75 and 2.95 on the rear face, in comparison to the measured values of 5.2 to 6.6 on the front face and 4.1 to 6.2 on the rear face. This discrepancy is due to non-Gaussian nature of the experimental data.

7.4. Codification of wind loading data

The objective of wind loading codes of practice is to determine the extreme gust value acting on a specific structure. The current UK code, BS6399 (British Standard 1997) is typical of modern codes. Inevitably this code contains a number of assumptions, and the wall data discussed in this paper enable some of these assumptions to be checked. Specifically in what follows we will consider three such assumptions as follows.

a) the assumption that the k values in the empirical fit to the coherence values (Eq. 6) is constant at 4.5;
b) the assumption that the "pseudo-steady" values of pressure coefficient are close to and have a simple one to one relationship with the mean pressure coefficients;
c) the assumption that the lack of correlation between the pressure forces on the front and rear of the structure can be allowed for by a simple empirical correction.

We consider first assumption (a). A fundamental assumption that underlies BS6399 is that the averaging time τ_a can be related to the significant dimension of the loaded area L and the mean velocity U by

$$\tau_a = kL/U \tag{25}$$

where the value of k is taken from that in Eq. (6). The rationale for this is that this value of t represents the gust frequency at which the coherence falls to a value of e^{-1}. On the basis of the Royex House results (Newberry *et al.* 1973) a value of 4.5 is used. This rationale has met with very

severe criticism by Holmes (1995) and Dyrbe and Hansen (1999), who nonetheless recognise that the approach is an extremely attractive one due to its simplicity. On the basis of a consideration of aerodynamic admittances they suggest that this approach can be used, with caution, with rather lower values of k. Here we do not enter into this particular argument (although the author's sympathy is with the work of Holmes) and restrict ourselves to a consideration, or otherwise, of whether k is constant at 4.5. Clearly Fig. 13 and Table 2 show that, for the wall data, k is far from being a constant. If a single value is required, then the lowest measured value should be chosen (around 2.0) since this represents the most conservative assumption with the greatest coherence values.

The second aspect of the code that will be investigated is the use the "pseudo-steady" pressure coefficient. This is defined as

$$C_{pps} = \frac{(p_e - p_r)}{0.5\rho U_e^2} \tag{26}$$

where the subscript e again refers to the extreme value. Cook (1990) shows that such a coefficient is usually numerically close to the mean coefficient and is thus extremely convenient for use in codes, where existing mean pressure coefficient data can be replaced gradually as pseudo-steady coefficient data becomes available, with no change to the code format. Fig. 25 shows the ratio of the pseudo-steady pressure to the mean pressure coefficient, defining the extreme value as the maximum 1.8s value. For the current data the values of this ratio are generally greater than 1 on the front face and less than 1 on the rear face. Paradoxically Cook argues that values of less than 1 indicate that not all velocity fluctuations contribute to the surface pressure fluctuations (and such a ratio could be expected on windward walls), whilst values greater than 1 indicate turbulence induced by separated flows - i.e., in wakes or separation bubbles. This is exactly the opposite of what the current results suggest, and the discussion of section 7.2 suggests the truth is somewhat more complex. Also it is straightforward to show that this ratio of pseudo steady coefficient to mean coefficient is equal to the ratio of the quantile level pressure coefficient and the quasi-steady pressure coefficient defined in the last section. An examination of the results of Figs. 24 and 25 shows that they are consistent in this regard.

Finally Fig. 26 shows the non-correlation factor between the front and rear faces K. This is defined the maximum 1.8s value of the net pressure coefficient across the wall to the difference between the corresponding values for the front and rear faces. The UK code suggests a universal value of 0.85 for this parameter. It can be seen to be less than 1.0 (usually around 0.85 to 0.9) which indicates that the peak events on the front and rear faces are not fully correlated and that the suggested value is a reasonable approximation.

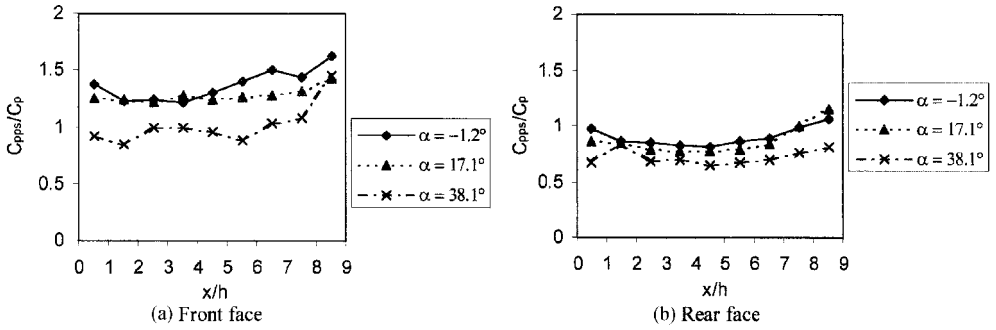

Fig. 25 Ratio of pseudo-steady to mean pressure coefficients

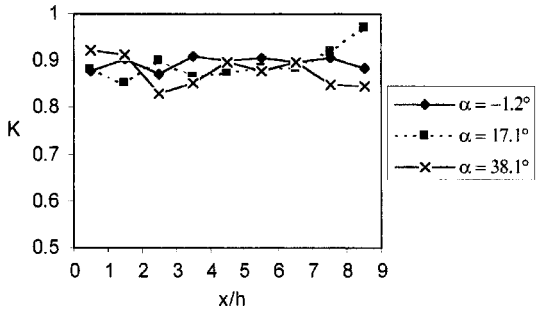

Fig. 26 Non-correlation factor

8. Conclusions

From the results that have been presented in earlier sections the following conclusions can be drawn.

(a) Even though the flow geometry is one of the simplest that can exist, the nature of the unsteady flow field is complex.
(b) The fluctuating pressures on the front face of the wall are to a great extent caused by the turbulent fluctuations in the upstream flow, and reflect the oncoming flow structures. The results suggest that there are two major scales in the oncoming flow - one with a period in the region of 100s (which probably scales on atmospheric boundary layer thickness) and a much smaller scale with a period of the order of 1 second. The peak pressure events represent a superposition of the maxima of these two scales of fluctuation. In general the quasi-steady approach can adequately relate the fluctuating pressures to the fluctuating velocities.
(c) The fluctuating pressures on the rear face are also influenced by the fluctuations in the oncoming turbulence, but also by unsteady fluctuations due to wake unsteadiness. The rear face fluctuations have a greater temporal and spatial coherence than the front face fluctuations at all scales, and the extreme events are significantly longer than on the front face. The quasi-steady method overpredicts the rear face unsteadiness, which suggests that the effect of the wake is to partly damp out the quasi-steady effects.
(d) The UK code values for the "*k*" parameter have been shown to be too high for the data considered here, and the use of pseudo-steady coefficients has also been shown not to be entirely adequate. The non-correlation factor *K* does however appear to be adequate.

Acknowledgements

The author would like to acknowledge the help and advice of staff at Silsoe Research Institute, and in particular Dr R. Hoxey and Mrs. L. Short who put the experimental data into a form suitable for analysis.

References

Baker, C. J. (2000), "Aspects of the use of proper orthogonal decomposition in the analysis of surface pressure fields", *Wind and Structures, An lnt. J.* **3**(2), 97-115.

BSI (1997), "Loadings for buildings; code of practice for wind loads", British Standard BS6399.
Cook, N. J. (1990), "The designers guide to wind loading of building structures - static structures", BRE/ Butterworths.
Dyrbye, C. and Hansen, S. O. (1999), *Wind Loads on Structures*, Wiley.
ESDU (1985), "Characteristics of atmospheric turbulence near the ground; Part 2 Single point data for strong winds - neutral atmosphere", Data Item 85020, Engineering Sciences Data Unit, London.
Gurley, K. and Kareem, A. (1999), "Applications of wavelet transforms in earthquake, wind and ocean engineering", *Eng. Struct*., **21**, 149-167.
Holmes, J. D. (1990), "Analysis and synthesis of pressure fluctuations on bluff bodies using eigenvectors", *J. Wind Eng. Ind. Aerod*, **33**, 219-230.
Holmes, J. D. (1995), "Equivalent time averaging in wind engineering", *Proc. of the 9th Int. Conf. on Wind Eng*., Dehli, 1849-1858.
Hoxey, R. P. and Richards, P. J. (1992), "Structure of the atmospheric boundary layer below 25 m and implications to wind loading on low rise buildings", *J. Wind Eng. Ind. Aerod*., **41-44**, 317-327.
Hoxey, R. P., Richards, P. J., Richardson, G. M., Robertson, A. P. and Short, J. L. (1996), "The folly of using extreme value methods in full scale experiments", *J. Wind Eng. Ind. Aerod*., **60**, 109-122.
Hoxey, R., Short, L. and Richards, P. (1999), "Quasi-steady theory developed with experimental verification", Wind Engineering in the 21st Century, Eds Larsen, Larose and Livesy, Balkema, Rotterdam, *Proc. 10th Int. Conf. on Wind Eng*., 1679-1686.
Jordon, D. A., Hajj, M. R. and Tieleman, H. W. (1997), "Characterisation of turbulence scales in the atmospheric surface layer with the continuous wavelet transform", *J. Wind Eng. Ind. Aerod*., **69-71**, 709-716.
Jordon, D. A., Hajj, M. R., Miksad, R. W. and Tieleman, H. W. (1999), "Analysis of the velocity pressure peak relation for wind loads on structures", Wind Engineering in the 21st Century, Eds Larsen, Larose and Livesy, Balkema, Rotterdam, *Proc. 10th Int. Conf. on Wind Eng*. 443-448.
Kareem, A. (1997), "Correlation structure of random pressure fields", *J. Wind Eng. Ind. Aerod*., **69-71**, 507-516.
Letchford, C. W. and Holmes, J. D. (1994), "Wind loads on free standing wall in turbulent boundary layers", *J. Wind Eng. Ind. Aerod*., **51**, 1-27.
Letchford, C. W., Iverson, R. E. and McDonald, J. R. (1993), "The application of quasi-steady theory to full scale measurements on the Texas Tech Building", *J. Wind Eng. Ind. Aerod*., **48**, 111-132.
Letchford, C. W. and Mehta, K. C. (1993), "The distribution and correlation of fluctuating pressures on the Texas Tech Building", *J. Wind Eng. Ind. Aerod*., **50**, 225-234.
Newberry, C. W., Eaton, K. J. and Mayne, J. R. (1973), "Wind loading on tall buildings - further results from Royex House", Buidling Research Establishment Current Paper 29/73 HMSO.
Richards, P. J., Fong, S. and Hoxey, R. P. (1997), "Anisotropic turbulence in the atmospheric surface layer", *J. Wind Eng. Ind. Aerod*., **69-71**, 903-913.
Robertson, A. P., Hoxey, R. P., Short, J. L., Ferguson, W. A. and Blackmore (1996a), "Wind loads on boundary walls - full scale studies", *J. Wind Eng. Ind. Aerod*., **69-71**, 451-459.
Robertson, A. P., Hoxey, R. P., Short, J. L., Ferguson, W. A. and Osmond, S. (1996b), "Full scale testing to determine the wind loads of free standing walls", *J. Wind Eng. Ind. Aerod*., **60**, 1-3, 123-137.
Robertson, A. P., Hoxey, R. P., Short, J. L., Ferguson, W. A. and Blackmore (1997), "Prediction of structural loads from fluctuating wind pressures - validation from full scale forces and pressure measurements", Proc. 2nd European and African Conference on Wind Engineering 1007-1014.
Tamura, Y., Suganamu, S., Kikuchi, H. and Hibi, K. (1999), "Proper orthogonal decomposition of random wind pressure field", *J. Fluid. Struct.*, **13**, 1069-1095.
Torrence, C. and Compo, G. P. (1998), "A practical guide to wavelet analysis", *Bulletin of the American Meteorological Society*, **79**(1), 61-78.

Notation

C	Cross correlation function
Co_{cpij}	Pressure coefficient coherence between points i and j
C_p	Pressure coefficient

C_{pcs}	Conditionally sampled pressure coefficient
C_{pe}	Extreme value of pressure coefficient
C_{pps}	Pseudo-steady value of pressure coefficient
F	Autocorrelation function
f	Frequency
g_{cp}	Pressure coefficient gust factor
h	Wall height
k	Factor in coherence curve fit
K	Non correlation factor
p	Pressure
p_e	Extreme value of pressure
p_r	Reference pressure
P_i	POD mode spatial function
R	Ratio of wavelet power spectrum at extreme event to average wavelet power spectrum
s	Wavelet scale
s_{cp}	Skewness of pressure coefficient
s_q	Skewness of dynamic pressure
s_u, s_v, s_w	Skewness of velocity components
S_{cp}	Spectral density of pressure coefficient
S_u, S_v, S_w	Spectral density of velocity components
S_{Ti}	Spectral density of mode temporal function
t	Time
T	Dimensionless period of extreme event
T_i	POD mode temporal function
T_o	Observation period
u	Longitudinal velocity component
u_τ	Shear velocity
U	Mean reference velocity
U_e	Extreme value of reference velocity
v	Lateral velocity component
w	Vertical velocity component
$w_{cp}(s, n)$	Wavelet transform of pressure coefficient
$W_{cp}(s, n)$	Wavelet spectrum of pressure coefficient
$W_{cp}(s)$	Average value of wavelet spectrum
x	Distance from end of wall
X_{Cp}	Pressure coefficient admittance
X_{Ti}	POD temporal function admittance
X_{WCp}	Pressure coefficient wavelet spectrum admittance
y	Separation between two pressure taps
α	Lateral wind angle
β	Vertical wind angle
δt	Time increment in wavelet analysis
ν	Zero crossing rate
ρ	Density of air
τ	Time lag
τ_a	Averaging time
σ_{Cp}	Standard deviation of pressure coefficient
σ_u, σ_v, σ_w	Standard deviation of velocity components
ψ	Wavelet function
ψ_0	Normalised wavelet function
ω_0	Parameter in wavelet analysis